Opacity and conductivity measurements in noble gases at conditions of planetary and stellar interiors

R. Stewart McWilliams[a,b,c,d,e,1], D. Allen Dalton[a], Zuzana Konôpková[f], Mohammad F. Mahmood[a,e], and Alexander F. Goncharov[a,g]

[a]Geophysical Laboratory, Carnegie Institution of Washington, Washington, DC 20015; [b]School of Physics and Astronomy, University of Edinburgh, Edinburgh EH9 3FD, United Kingdom; [c]Centre for Science at Extreme Conditions, University of Edinburgh, Edinburgh EH9 3FD, United Kingdom; [d]Departamento de Geociencias, Universidad de Los Andes, Bogotá DC, Colombia; [e]Department of Mathematics, Howard University, Washington, DC 20059; [f]Deutsches Elektronen-Synchrotron Photon Science, 22607 Hamburg, Germany; and [g]Key Laboratory of Materials Physics, Institute of Solid State Physics, Chinese Academy of Sciences, Hefei 230031, China

The noble gases are elements of broad importance across science and technology and are primary constituents of planetary and stellar atmospheres, where they segregate into droplets or layers that affect the thermal, chemical, and structural evolution of their host body. We have measured the optical properties of noble gases at relevant high pressures and temperatures in the laser-heated diamond anvil cell, observing insulator-to-conductor transformations in dense helium, neon, argon, and xenon at 4,000–15,000 K and pressures of 15–52 GPa. The thermal activation and frequency dependence of conduction reveal an optical character dominated by electrons of low mobility, as in an amorphous semiconductor or poor metal, rather than free electrons as is often assumed for such wide band gap insulators at high temperatures. White dwarf stars having helium outer atmospheres cool slower and may have different color than if atmospheric opacity were controlled by free electrons. Helium rain in Jupiter and Saturn becomes conducting at conditions well correlated with its increased solubility in metallic hydrogen, whereas a deep layer of insulating neon may inhibit core erosion in Saturn.

rare gases | extreme conditions | warm dense matter | giant planet | white dwarf

Noble gases play important roles in the evolution and dynamics of planets and stars, especially where they appear in a condensed, purified state. In gas giant planets, helium and neon can precipitate as rain in metallic hydrogen envelopes, leading to planetary warming and specifically the anomalously slow cooling of Saturn (1–8). In white dwarf stars cooling can be especially fast due to the predicted low opacity of dense helium atmospheres, affecting the calibration of these objects as cosmological timekeepers (9–12). In these systems, the transformation of dense noble gases (particularly He) from optically transparent insulators to opaque electrical conductors is of special importance (2, 9, 11, 12).

Dense noble gases are expected to show systematic similarities in their properties at extreme conditions (13–17); however, a general understanding of their insulator–conductor transformation remains to be established. Xe is observed to metallize near room temperature under pressures similar to those at Earth's core–mantle boundary (18, 19). Ar and He are observed to conduct only at combined high pressure and temperature (12, 13, 17). Ne is predicted to have the highest metallization pressure of all known materials—10^3 times that of Xe and 10 times that of He (14, 18, 20, 21)—and has never been documented outside of its insulating state. Experimental probes of extreme densities and temperatures in noble gases have previously relied on dynamic compression by shock waves (12, 13, 17, 22–24). However, in such adiabatic experiments, light and compressible noble gases heat up significantly and can ultimately reach density maxima (12, 13, 17, 21, 24, 25), so that conditions created often lie far from those deep within planets (7, 8) and stars (9).

Here we report experiments in the laser-heated diamond anvil cell (15, 16, 26–29) on high-density and high-temperature states of the noble gases Xe, Ar, Ne, and He (Fig. 1). Rapid heating and cooling of compressed samples using pulsed laser heating (26, 27) is coupled with time domain spectroscopy of thermal emission (26) to determine sample temperature and transient absorption to establish corresponding sample optical properties (Figs. S1 and S2). A sequence of heat cycles to increasing temperature documents optical changes in these initially transparent insulators.

Results

Time domain spectroscopic data on pulsed heated samples are presented in Figs. 2 and 3. Absorption coefficients are determined as

$$\alpha = -\ln(I_H/I_C)/d, \qquad [1]$$

where I_C and I_H are the transmitted probe intensity through cold (transparent) and hot samples, respectively, and d is the time-dependent thickness of the absorbing region, typically 4 ± 2 μm (Fig. 1C and Fig. S3). The corresponding conductivity is given as

$$\sigma = n\alpha c\varepsilon_0 \qquad [2]$$

for high frequencies, where n is the index of refraction (of order 1), c is the speed of light, and ε_0 is the permittivity of free space. Conductivity at low frequency was determined from shock

Significance

Planets and stars contain matter at extreme pressures and temperatures hidden deep beneath their opaque surfaces. Unable to see these states of matter directly, we instead produce them in laboratory experiments. Here a novel method of studying extreme states in a tabletop experiment is described and applied to common planet- and star-forming materials, the noble gases. Helium, neon, argon, and xenon transform in the experiments from transparent electrical insulators to opaque electrical conductors. In Saturn, rain composed of noble gas becomes conductive as it falls and can form a protective layer around the planetary core that prevents the core from dissolving into surrounding metallic hydrogen. White dwarf stars have unexpectedly opaque helium atmospheres, causing them to age slower than anticipated.
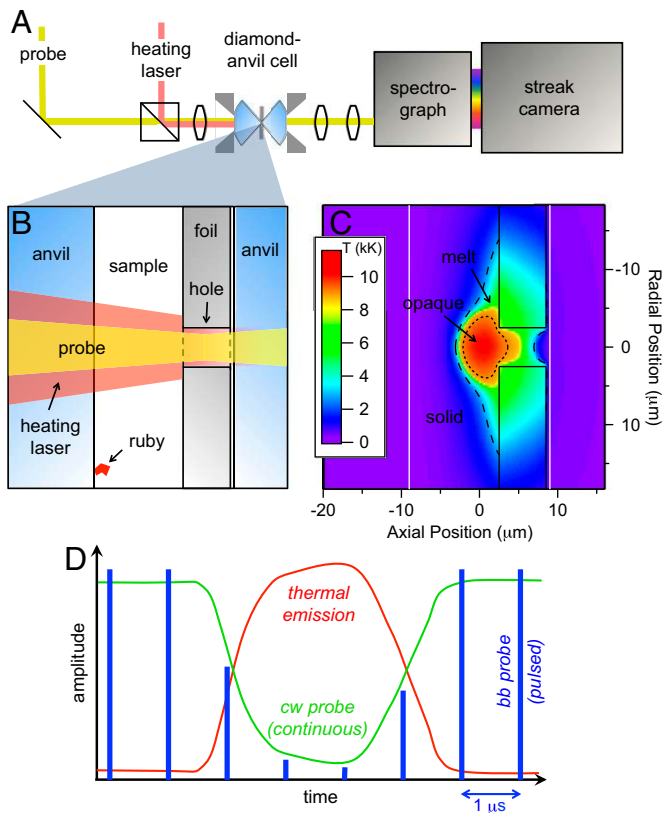
PHYSICS

Fig. 1. Creating and probing extreme states of noble gases. (*A*) Configuration of laser heating and transient absorption probing of the diamond anvil cell, with probe beams transmitted through the cell into the detection system. (*B*) Microscopic view of the diamond cell cavity, which contains a noble gas sample and a metal foil (Ir) which converts laser radiation to heat and has small hole at the heated region through which probe beams are transmitted to test optical character of samples. (*C*) Finite element model (26) ([Fig. S3](#)) of the temperature distribution in heated Ar at 51 GPa (Fig. 2), with solid–melt (16) and insulator–conductor ($\alpha = 0.1 \ \mu m^{-1}$) boundaries in the sample marked dashed and dotted, respectively. (*D*) Schematic of time domain probing during transient heating. Temperature is determined from thermal emission (red) and absorption from transmitted probe beams: a continuous laser (cw; green) and pulsed supercontinuum broadband (bb; blue).

wave direct current (DC) conductivity data (where available; *SI Text*).

The onset of absorption occurs at temperatures well above noble gas melting points (15, 16) and so in fluid states (Fig. 4). Electronic band gaps (E_g) at these conditions are larger than the energies of light used, ruling out direct interband (bound-free) absorption. Optical changes due to thermally excited free electrons, often believed to dominate in dense insulators at high temperatures (2, 9, 11, 12, 30), yield a simple criterion for the temperature of optical transformation and absorption onset, based on Drude free electron behavior in a semiconductor (12, 30) (*SI Text*). However, strong absorption appears at lower temperature than expected from this model, at conditions where free electron absorption should be small to negligible. For example, in Ar at 51 GPa (Fig. 2), the band gap is 7.4 eV, whereas our spectral range is below 2.7 eV, ruling out interband absorption. High absorption ($\alpha > 0.1 \ \mu m^{-1}$) is observed above 6,700 K (0.6 eV). At this temperature the DC conductivity is ~1 S/cm (12, 13, 17, 30, 31) (*SI Text*), but the corresponding free electron absorption (~0.01 μm^{-1}) is an order of magnitude lower than the observed absorption.

Across all noble gases studied, the temperature T_C for the onset of high absorption increases systematically with the band gap E_g as

$$kT_C \approx 0.078 \ E_g, \qquad [3]$$

where *k* is Boltzmann's constant, defining a global transformation boundary (Fig. 5). This dependence is similar to that predicted by free electron theory ($kT_C \sim 0.071 \ E_g + 0.33$ eV; Fig. 5) but is offset to lower temperature by several thousand degrees K.

Direct measurements of absorption spectra (Fig. 2) provide a clear insight into the nature of the opaque high-temperature state. Rather than showing absorption (Fig. 2*E*) and conductivity (Fig. 2*F*) decreasing with photon energy, as expected for free electron optical character (9, 11, 18, 32, 33), these quantities increase. Optical conductivity is high compared with the DC conductivity but of similar magnitude.

The data thus evince an enhancement of conduction with temperature; however, free electrons do not describe its spectral character or thermal activation behavior.

Discussion

As interband excitations do not account for the optical changes observed here, other explanations must be examined. Absorption may be dominated by localized states within the band gaps, a common trait of disordered semiconductors associated with a characteristic Urbach absorption behavior (33, 34), which well describes our data (Fig. 2*E* and *SI Text*). Orbital-hybridized or charge-sharing clusters in the fluid (11, 15, 35) could provide a localized basis of absorption (34). First-principles electronic structure models for warm dense noble gases should thus not neglect localization effects a priori (2). Data are also well described by a common conductivity model for a poor metal with low electron mobility (32) (Fig. 2*F*), which reproduces the weakly increasing conductivity from DC to optical frequencies and predicts a maximum in conductivity at finite frequency. Such features also characterize other warm dense matter near metallization transitions, including hydrogen (36), aluminum (37), and mercury (32). Indirect-gap (18) and Tauc (33) absorption behaviors, known to occur in rare gas solid and disordered semiconductors, respectively, could not describe these data self-consistently (*SI Text*).

Ar and Xe show significant reductions in transformation temperature with increasing pressure (Fig. 4), consistent with the high sensitivity of the band gaps to compression (18, 38–41) ([Figs. S4](#) and [S5](#)). At higher pressures, fluid Ar and Xe should transform to conductors upon melting: from Eq. 3, fluid Xe is conducting along the melting curve (15, 16) above ~60 GPa and fluid Ar (16) above ~160 GPa (Fig. 4). This confirms that anomalous melting behavior in Xe under pressure (15, 16) can be attributed to electronic transformation in the fluid (15) and suggests anomalous thermal emission reported from laser-heated Ar near melting, at 90 GPa and ~4,500 K (29), could be due to opacity of hot Ar. He and Ne require the highest temperatures to exhibit optical darkening, of 10,000–12,000 K and 15,000–18,000 K, respectively, confirming the especially insulating character predicted for Ne (14, 20, 21). Due to the relative insensitivity of He and Ne band gaps to changes in density (2, 11, 14, 20, 25, 30) ([Fig. S6](#)), these threshold temperatures should be similar over a wide domain of pressures in planetary (6–8) and stellar (9, 10) interiors (Fig. 4 and *SI Text*).

White dwarf stars possess dense atmospheres of He at conditions directly probed in our experiments (9–12) (Figs. 4 and 5). Our measurements affirm that these atmospheres are highly transparent at visible and near-IR wavelengths, a feature believed to produce particularly rapid stellar cooling due to efficient transport of thermal radiation (9, 10, 12). However, atmospheric opacity will be higher than if caused by free electrons (Fig. 5), implying relatively slower cooling (9, 10). An atmospheric opacity increasing toward the blue (e.g., Fig. 2) rather than the red as predicted by free electron models (9, 11) could lead to
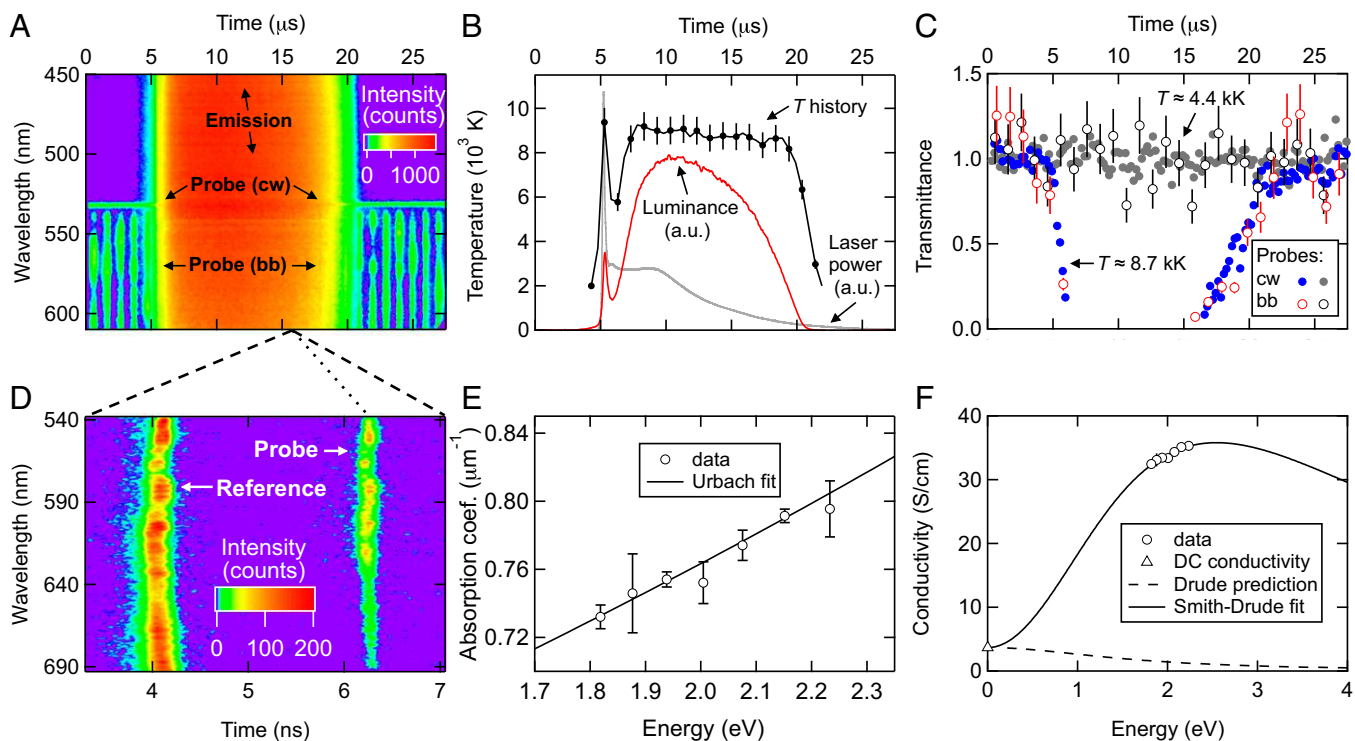
Fig. 2. Absorption and conduction in argon at 51 GPa. (*A*) Spectrogram of emission and transient absorption using continuous monochromatic (cw) and pulsed broadband (bb) (48) probes during a heat cycle (method of Fig. 1). (*B*) Temperature history with uncertainty, thermal luminance, and laser power for *A*. (*C*) Sample transmittance (532–615 nm) for *A* and at a lower temperature (bb error bars are uncertainty due to broadband source power). (*D*) Spectrogram of transient absorption (bb) during a heating event similar to *A* but taken on a faster timescale to remove thermal background and including one probe pulse and its reference. (*E*) Absorption spectrum derived from *D* assuming a 4-μm-thick absorbing sample and fit to a semiconductor Urbach (33) model (error bars are standard deviation from three spectra). (*F*) Conductivity spectrum derived from *E*, the optical index of refraction (50, 53), and the DC conductivity (12, 13, 17, 30), with metallic Drude (12, 30) and poor-metal Smith–Drude (32) models.

deficiencies in blue color (9), which have been documented in a subset of white dwarfs (9).

Significant theoretical and observational evidence for phase separation of helium and neon in the hydrogen-rich outer envelopes of giant planets has been reported (1–8), yet questions over the nature and even existence of this phase separation remain (2, 42, 43). This is in part due to limited direct experimental data on the hydrogen–helium–neon system at the conditions of phase separation: although hydrogen is observed in a metallic state at the interior conditions of giant planets (44), measurements on the electronic character of helium and neon at relevant densities and temperatures have been limited (12, 13, 17, 45). As phase separation may be controlled by the electronic properties of the constituents (1, 2, 4), the present measurements have a direct bearing on this problem.

Our measurements show that in Saturn above ~0.25 of the planet's radius (R_S) and in Jupiter above ~0.70 of its radius (R_J), precipitated He would be insulating (Fig. 5). He droplets would be weakly conducting below these depths and to the core–envelope boundary of Saturn, lying just beyond the transformation at ~0.15 R_S. In Jupiter, phase-separated He would transform further at depth, developing metallic properties (12, 30) below ~0.25 R_J and above the core surface at ~0.10 R_J.

However, the onset of conducting states observed here closely corresponds with the conditions where helium is predicted (3, 4) to become fully soluble in metallic hydrogen (Fig. 5 and *SI Text*), consistent with expectations that electronic transformations and miscibility are related in hydrogen–helium mixtures (1, 2, 4). In Saturn, for example, the maximum temperature of immiscibility is predicted at 8,000 ± 800 K (3, 4), whereas electronic transformation has progressed significantly by ~9,800 K (Fig. 5). The

thermal production of singly ionized He, a chemical species isoelectronic with atomic hydrogen that is a likely source of observed optical and electronic changes (9, 11, 25), is one possible cause of increased miscibility. The data also highlight the importance of localized rather than extended electronic changes in the warm dense noble gases, which may play an important role in chemical behavior. He electronic change has sometimes been expected to be not relevant to the miscibility question, on the argument that He remains insulating near demixing conditions (3, 43); the data confirm this not to be the case. If He electronic changes controlled miscibility, then the insensitivity of He electronic properties to pressure (2, 11, 14, 25, 30) (Fig. 4 and Fig. S6) would imply pressure independence in the maximum temperature of immiscibility, as seen in recent theory (3, 4) at high pressures (*SI Text*).

Based on these considerations, phase separated He should tend to dissolve just above Saturn's core (Fig. 5). However, unlike He, Ne remains an insulator at core conditions in Saturn ($T < 11,000$ K). If Ne exhibited a correlation between its electronic character and mixing behavior similar to that indicated for He, then Ne sequestered and concentrated by He rain in the deep interior (1, 5) may remain exsolved even if He is dissolved. Thus, noble gas precipitate could accumulate on the core surface (7, 8), even in the event of He dissolution. This noble gas layer, chemically unreactive with metallic hydrogen, would inhibit erosion (6, 8, 46) of the underlying core, even if very thin (*SI Text*). Although plausible for Saturn, such a layer is unlikely for Jupiter, given the insulator-to-conductor transformations of both He and Ne at the temperature of Jupiter's core. This could contribute to differential core erosion in these planets and so to the differences in their core size, envelope heavy element
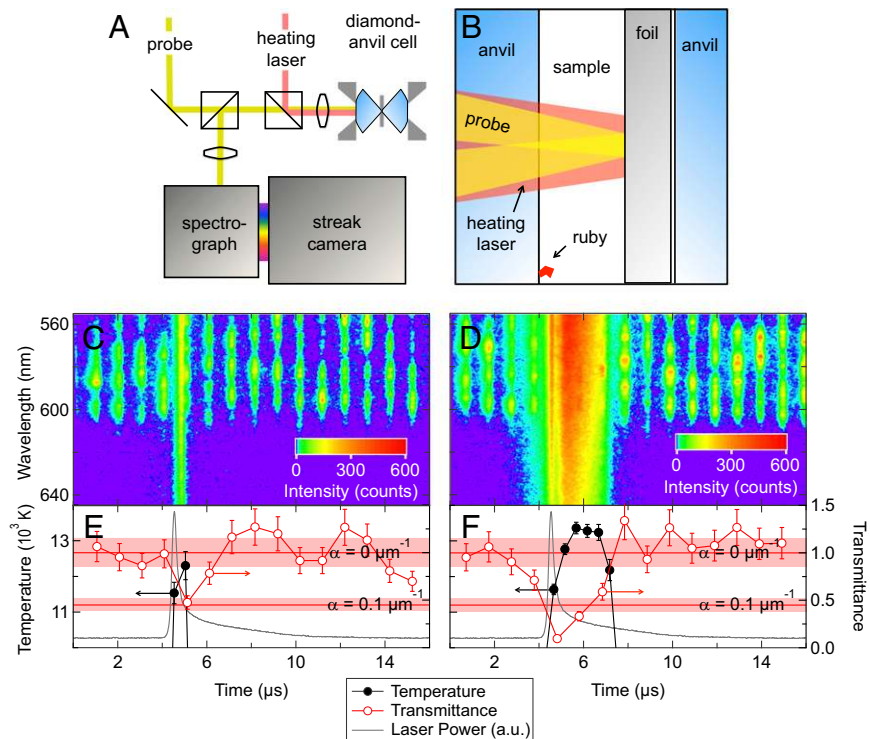
Fig. 3. Absorption onset in helium at 22 GPa. (*A*) Configuration of laser heating and transient absorption with probe beams reflected in the diamond cell. (*B*) Microscopic view of the cavity, where probe beams are reflected from the foil surface in a laser heated area. (*C* and *D*) Spectrograms for transparent and absorbing samples, respectively, with broadband probing. (*E* and *F*) Sample temperature (black points, left axes) and transmittance (red points, right axes) shown with transmission levels (horizontal lines) for $\alpha = 0$ and $\alpha = 0.1$ μm^{-1} (red error bars and bands are uncertainty due to broadband source power). From *C* and *E* to *D* and *F*, absorption increases concomitantly with emission intensity, duration, and temperature. A 4-μm-thick absorbing sample and two-pass absorption is used to compute α.

enrichment, and luminosity (3, 4, 6–8). Saturn and Jupiter may thus lie at a boundary between internally condensed and internally mixed gas giants controlled by formation of a protective noble gas envelope around the cores of cooler planets.

Materials and Methods

Diamond anvils with 300-μm-diameter flat culets were used, with Re gaskets, pressure-loaded ultrahigh purity noble gases, and Ir laser-coupling foils; sample pressure was determined via ruby fluorescence (47). Confocal optical spectroscopy (Fig. S1) is used to record visible spectra from the IR (1,075 nm) laser-heated sample (27). In place of a CCD (27), a streak camera is mounted to the spectrometer to record spectra continuously during heating cycles,

producing spectrograms of emission and transient absorption (Figs. 2 and 3). Thermal emission is detected as broadband and temporally continuous signal (Fig. 1D) and is fit to a Planck function to determine temperature (Fig. S2). Probe beams for transient absorption passing through the heated sample are detected simultaneously with emission but are discrete in either wavelength (green continuous laser) or time (pulsed supercontinuum broadband) (48) and are in this way discriminable from emission background (Fig. 1D). Laser heating pulses of several microseconds duration were used (26, 27).

Sample optical transformation was manifested by several concomitant changes in the spectrograms upon increasing laser power (*SI Text*): (*i*) a sudden enhancement of transient absorption and (*ii*) a shift to higher temperature, emission intensity, and heat cycle duration. These phenomena are attributed
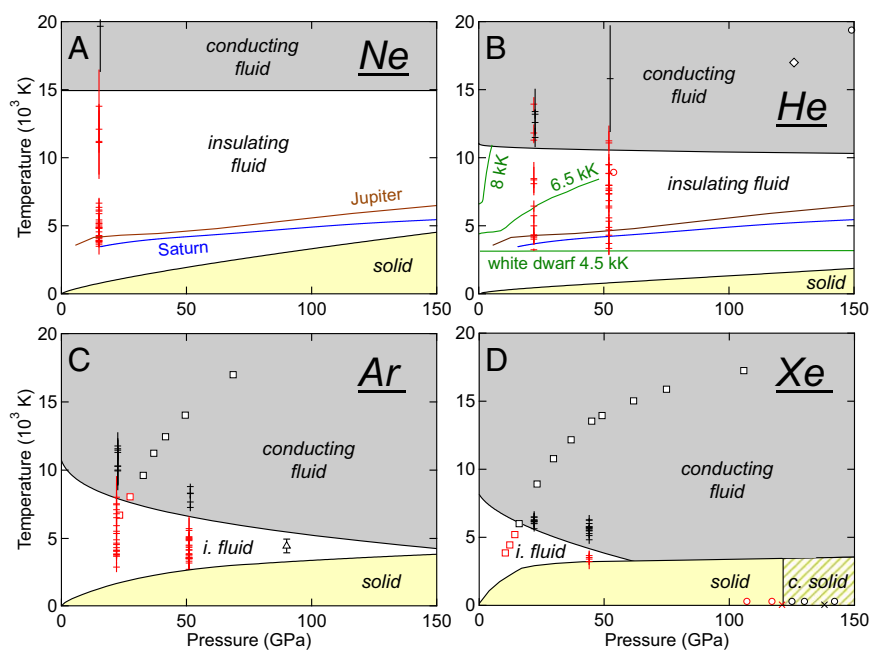

Fig. 4. Phase diagrams of Ne (*A*), He (*B*), Ar (*C*), and Xe (*D*) from experimental measurements. Present measurements of optical absorption are horizontal dashes (red, $\alpha < 0.1$ μm^{-1}; black, $\alpha > 0.1$ μm^{-1}); vertical bars represent the range of temperatures observed in each material state, plus uncertainty (Fig. S7). Black lines are phase boundaries for fluid–fluid insulator–conductor transformation (Eq. 3), melting (15, 16) and solid–solid insulator–conductor transformation in Xe (18, 19). Prior data are squares (conductivity) (13, 17, 22, 54) or circles (absorptivity) (12, 18) with red indicating $\sigma < 1$ S/cm, $\alpha < 0.1$ μm^{-1}, and black indicating $\sigma > 1$ S/cm, $\alpha > 0.1$ μm^{-1}; black triangle is region of anomalous emission in Ar (29); red (black) crosses indicate insulating (metallic) electrical behavior in Xe (19); and black diamond indicates dense plasma conditions in He (24). Also shown are interior conditions of Jupiter (brown) (6), Saturn (blue) (7), and white dwarfs (green) for effective temperatures of 8.0, 6.5, and 4.5×10^3 K (9).
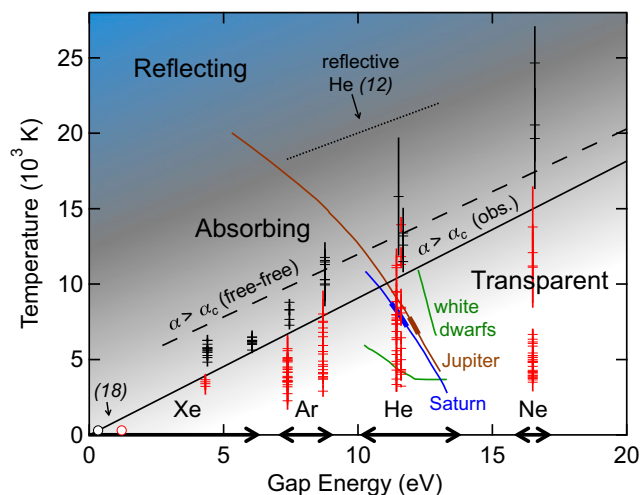
Fig. 5. Optical properties of noble gases at 450–1,075 nm as a function of band gap. Absorption coefficients α below (red) or above (black) the critical value ($\alpha_c = 0.1\ \mu\mathrm{m}^{-1}$) are from this study (horizontal dashes) on fluid Ne (15 GPa), He (22, 52 GPa), Ar (22, 51 GPa), and Xe (22, 44 GPa) and prior work (circles) on solid Xe (120 GPa) (18). Corresponding band gaps are estimated at the conditions of optical transformation. The data define a boundary of linear character (black solid line; Eq. 3) where conductivities are ~1 S/cm. The free electron model (12, 30) location of this boundary is the dashed black line (*SI Text* and Fig. S7). High reflectivity (>1%) and conductivity (>100 S/cm) occur above the dotted black line (12, 23, 30). Colored lines are conditions of He atmospheres of white dwarfs (9, 30) (green; for effective temperatures 8.0 and 4.5 kK) and He rain in planetary gaseous envelopes (blue and brown) (6, 7, 25, 30) with thicker areas indicating predicted upper limit of He–H immiscibility (3, 4).

to broadband (visible to IR) enhancement in sample optical absorptivity and emissivity such that the efficiency of incident heating laser absorption increases (28) together with probe absorption.

Broadband transient absorption probe data include uncertainty due to random pulse spectral intensity variation (48) (Figs. 2*C* and 3 *E* and *F*), or these variations were cancelled out by pulse referencing (Fig. 2*E*). The broadband probe was often edge-filtered (Figs. 2*A* and 3 *C* and *D*) to reserve a portion of the spectrogram for measurement of emission alone. Probing was made by reflecting beams from the metallic (reflective) foil in a laser-heated area and through overlying hot sample (Fig. 3) or by transmitting beams through a small hole in the foil at the laser heated area (Figs. 1 and 2). The critical α of 0.1 $\mu\mathrm{m}^{-1}$ ($\sigma \sim 1$ S/cm; Eq. 2) is roughly the detection limit for absorbing conditions, above which sample transformation was clearly evident (Fig. 3).

Band gaps for noble gases Xe, Ar, and He were estimated at the volume (31, 45, 49, 50) and temperature of optical transformation using experimental (12, 13, 17, 18, 31, 38, 51, 52) and theoretical (2, 11, 30, 39–41) results (Figs. S4–S7 and *SI Text*). The Ar gap was modeled as (Fig. S4)

$$E_g = 18.5 - 75.6\ V^{-0.926} - 0.000527\ T^{0.902},\qquad [4]$$

and the Xe gap was modeled as (Fig. S5)

$$E_g = 10.2 - 601\ V^{-1.74},\qquad [5]$$

with E_g in eV, V in cm^3/mol, and T in K. The gap variation in He was estimated from a prior model (30). The gap of Ne is less well known and was estimated from its initial value (20) and assuming a temperature sensitivity similar to He (Figs. S6 and S7 and *SI Text*), giving $E_g \approx 16.5$ eV. Uncertainties in band gap estimates (Fig. S7) are small compared with the variation across the noble gases and are accounted for in our conclusions. For example, the increase in temperature of absorption onset with band gap is well constrained.

Detailed methods can be found in *SI Text*.

1. Stevenson DJ (1998) States of matter in massive planets. *J Phys Condens Matter* 10(49):11227–11234.
2. Stixrude L, Jeanloz R (2008) Fluid helium at conditions of giant planetary interiors. *Proc Natl Acad Sci USA* 105(32):11071–11075.
3. Morales MA, et al. (2009) Phase separation in hydrogen-helium mixtures at Mbar pressures. *Proc Natl Acad Sci USA* 106(5):1324–1329.
4. Lorenzen W, Holst B, Redmer R (2009) Demixing of hydrogen and helium at megabar pressures. *Phys Rev Lett* 102(11):115701.
5. Wilson HF, Militzer B (2010) Sequestration of noble gases in giant planet interiors. *Phys Rev Lett* 104(12):121101.
6. Nettelmann N, Becker A, Holst B, Redmer R (2012) Jupiter models with improved ab-initio hydrogen equation of state. *Astrophys J* 750(1):52.
7. Nettelmann N, Pustow R, Redmer R (2013) Saturn layered structure and homogeneous evolution models with different EOSs. *Icarus* 225(1):548–557.
8. Guillot T (2005) The interiors of giant planets: Models and outstanding questions. *Annu Rev Earth Planet Sci* 33:493–530.
9. Bergeron P, Saumon D, Wesemael F (1995) New model atmospheres for very cool white-dwarfs with mixed H/He and pure He compositions. *Astrophys J* 443(2):764–779.
10. Fontaine G, Brassard P, Bergeron P (2001) The potential of white dwarf cosmochronology. *Publ Astron Soc Pac* 113(782):409–435.
11. Kowalski PM, Mazevet S, Saumon D, Challacombe M (2007) Equation of state and optical properties of warm dense helium. *Phys Rev B* 76(7):075112.
12. Celliers PM, et al. (2010) Insulator-to-conducting transition in dense fluid helium. *Phys Rev Lett* 104(18):184503.
13. Kuhlbrodt S, et al. (2005) Electrical conductivity of noble gases at high pressures. *Contrib Plasma Phys* 45(1):61–69.
14. Boettger JC (1986) Equation of state and metallization of neon. *Phys Rev B* 33(10):6788–6791.
15. Ross M, Boehler R, Söderlind P (2005) Xenon melting curve to 80 GPa and 5p-d hybridization. *Phys Rev Lett* 95(25):257801.
16. Santamaria-Perez D, Mukherjee GD, Schwager B, Boehler R (2010) High-pressure melting curve of helium and neon: Deviations from corresponding states theory. *Phys Rev B* 81(21):214101.
17. Fortov VE, et al. (2003) Pressure-produced ionization of nonideal plasma in a megabar range of dynamic pressures. *J Exp Theor Phys* 97(2):259–278.
18. Goettel KA, Eggert JH, Silvera IF, Moss WC (1989) Optical evidence for the metallization of xenon at 132(5) GPa. *Phys Rev Lett* 62(6):665–668.
19. Eremets MI, et al. (2000) Electrical conductivity of xenon at megabar pressures. *Phys Rev Lett* 85(13):2797–2800.
20. He YG, Tang XZ, Pu YK (2010) First-principle study of solid neon under high compression. *Physica B* 405(20):4335–4338.
21. Driver KP, Militzer B (2015) First-principles simulations and shock Hugoniot calculations of warm dense neon. *Phys Rev B* 91(4):045103.
22. Urlin VD, Mochalov MA, Mikhailova OL (1992) Liquid xenon study under shock and quasi-isentropic compression. *High Pressure Res* 8(4):595–605.
23. Reinholz H, et al. (2003) Frequency-dependent reflectivity of shock-compressed xenon plasmas. *Phys Rev E* 68(3 Pt 2):036403.
24. Zhernokletov MV, et al. (2012) Quasi-isentropic compression of dense gaseous helium at pressures up to 500 GPa. *JETP Lett* 96(7):432–436.
25. Militzer B (2009) Path integral Monte Carlo and density functional molecular dynamics simulations of hot, dense helium. *Phys Rev B* 79(15):155105.
26. Goncharov AF, et al. (2012) Thermal conductivity of argon at high pressures and high temperatures. *J Appl Phys* 111(11):112609.
27. Goncharov AF, et al. (2009) Laser heating in diamond anvil cells: Developments in pulsed and continuous techniques. *J Synchrotron Radiat* 16(6):769–772.
28. Boehler R, Ross M, Boercker DB (1997) Melting of LiF and NaCl to 1 Mbar: Systematics of ionic solids at extreme conditions. *Phys Rev Lett* 78(24):4589–4592.
29. Dewaele A, Mezouar M, Guignot N, Loubeyre P (2010) High melting points of tantalum in a laser-heated diamond anvil cell. *Phys Rev Lett* 104(25):255701.
30. Soubiran F, Mazevet S, Winisdoerffer C, Chabrier G (2012) Helium gap in the warm dense matter regime and experimental reflectivity measurements. *Phys Rev B* 86(11):115102.
31. Ross M, Mao HK, Bell PM, Xu JA (1986) The equation of state of dense argon: A comparison of shock and static studies. *J Chem Phys* 85(2):1028–1033.
32. Smith NV (2001) Classical generalization of the Drude formula for the optical conductivity. *Phys Rev B* 64(15):155106.
33. Mott NF, Davis EA (1979) *Electronic Processes in Non-Crystalline Materials* (Clarendon Press, Oxford), 2nd Ed.
34. Pan Y, Inam F, Zhang M, Drabold DA (2008) Atomistic origin of urbach tails in amorphous silicon. *Phys Rev Lett* 100(20):206403.
35. Kietzmann A, Holst B, Redmer R, Desjarlais MP, Mattsson TR (2007) Quantum molecular dynamics simulations for the nonmetal-to-metal transition in fluid helium. *Phys Rev Lett* 98(19):190602.

36. Collins LA, et al. (2001) Dynamical and optical properties of warm dense hydrogen. *Phys Rev B* 63(18):184110.
37. Desjarlais MP, Kress JD, Collins LA (2002) Electrical conductivity for warm, dense aluminum plasmas and liquids. *Phys Rev E* 66(2 Pt 2):025401.
38. Asaumi K, Mori T, Kondo Y (1982) Effect of very high-pressure on the optical-absorption edge in solid Xe and its implication for metallization. *Phys Rev Lett* 49(11):837–840.
39. Ross M, McMahan AK (1980) Condensed xenon at high-pressure. *Phys Rev B* 21(4):1658–1664.
40. Kwon I, Collins LA, Kress JD, Troullier N (1995) First-principles study of solid Ar and Kr under high compression. *Phys Rev B* 52(21):15165–15169.
41. Ross M (1968) Shock compression of argon and xenon. IV. Conversion of xenon to a metal-like state. *Phys Rev* 171(3):777–784.
42. Leconte J, Chabrier G (2013) Layered convection as the origin of Saturn's luminosity anomaly. *Nat Geosci* 6(5):347–350.
43. Morales MA, Hamel S, Caspersen K, Schwegler E (2013) Hydrogen-helium demixing from first principles: From diamond anvil cells to planetary interiors. *Phys Rev B* 87(17):174105.
44. Nellis WJ, Weir ST, Mitchell AC (1996) Metallization and electrical conductivity of hydrogen in Jupiter. *Science* 273(5277):936–938.
45. Dewaele A, Eggert JH, Loubeyre P, Le Toullec R (2003) Measurement of refractive index and equation of state in dense He, H2, H2O, and Ne under high pressure in a diamond anvil cell. *Phys Rev B* 67(9):094112.
46. Wahl SM, Wilson HF, Militzer B (2013) Solubility of iron in metallic hydrogen and stability of dense cores in giant planets. *Astrophys J* 773(2):5.
47. Mao HK, Xu J, Bell PM (1986) Calibration of the ruby pressure gauge to 800 kbar under quasi-hydrostatic conditions. *J Geophys Res* 91(B5):4673–4676.
48. Dudley JM, Genty G, Coen S (2006) Supercontinuum generation in photonic crystal fiber. *Rev Mod Phys* 78(4):1135–1184.
49. Makarenko I, Weill G, Itie JP, Besson JM (1982) Optical observations on xenon up to 63 GPa. *Phys Rev B* 26(12):7113–7115.
50. Hanna GJ, McCluskey MD (2010) Equation of state and refractive index of argon at high pressure by confocal microscopy. *Phys Rev B* 81(13):132104.
51. Steinberger IT, Asaf U (1973) Band-structure parameters of solid and liquid xenon. *Phys Rev B* 8(2):914–918.
52. Baldini G (1962) Ultraviolet absorption of solid argon, krypton, and xenon. *Phys Rev* 128(4):1562–1567.
53. Sinnock AC, Smith BL (1969) Refractive indices of condensed inert gases. *Phys Rev* 181(3):1297–1307.
54. Keeler RN, Royce EB (1971) Electrical conductivity of condensed media at high pressures. *Physics of High Energy Density*, eds Caldirola P, Knoepfel H (Academic, New York), Vol 48, pp 106–125.

Supporting Information

McWilliams et al. 10.1073/pnas.1421801112

Experimental Configuration

Diamond anvil culets were 300 μm flat, with gaskets of Re having cavities of 100 μm diameter, and were pressure-loaded with ultra high purity gases; Ir foil couplers were ~60 μm diameter, 6–12 μm thick, with holes of 5–15 μm diameter. Laser heating at 1,075 nm and spectroscopic imaging in the visible were achieved using a confocal optical system (1). Transient absorption spectroscopy (TAS) probing was introduced via the same confocal methods (Fig. S1). Probes consisted of a 1-MHz, 150-ps pulsed supercontinuum broadband (bb) (2) and a 532-nm continuous-wave laser (cw), each with a focal spot diameter of 5 μm at the sample, whereas the heating laser was focused to 10–20 μm, and emission measurements were localized to the probed region with spatial filtering. Spectrograms (Figs. 2 *A* and *D* and 3 *C* and *D*) were collected using a streak camera (Sydor ROSS 1000 with visible-band S20 intensifier) coupled to a spectrometer (Princeton f/4 with a 150 grooves/mm grating), having a 165-nm spectral window.

Data were obtained from a single shot (Figs. 2 *A* and *D* and 3 *C* and *D*) or by grouping data from similar shots (Fig. 2*E* and Fig. S2) to improve the signal-to-noise ratio or to extend the spectral range. TAS-bb data include uncertainty due to random source intensity variation (2) (Figs. 2*C* and 3 *E* and *F*) or used pulse referencing (Fig. 2*E*) so that these variations could be cancelled out in data processing; TAS-cw data used a source of constant intensity. TAS-bb was often dichroically edge-filtered so that only a portion of a spectral band was probed (the other portion being reserved for emission measurement) (Figs. 2*A* and 3). The discrete nature of the probes in time (bb) or wavelength (cw) allows them to be discriminated from emission background. In some cases, probe signal was too small relative to emission to be measured (e.g., middle of Fig. 2*A*). This was addressed by a faster sweep that collected less emission while preserving the intensity of the short-pulse (bb) probe (Fig. 2*D*). Heat cycle reproducibility was evaluated using emission, temperature, and TAS histories. Temperatures were measured by fitting emission to a Planck distribution in subranges of 500–800 nm with a time resolution of 0.5–2.0 μs (Fig. S2). States created during the heat cycles persist for timescales similar to or longer than those created by shock experiments (3–8), so thermodynamic equilibrium is also expected in the states observed here.

Criteria for Optical Transformation

At low laser power, the laser heats the foil directly while the sample is heated by conduction (1, 9). The onset of sample absorption with increasing power is identified by a decrease in probe transmittance to several percent or less and a concomitant increase in emission intensity, temperature, or duration of the high-temperature state (typically, all three occur concomitantly). Temperature histories also typically transition from closely following the heating laser power (9) to apparently decoupling from the laser power as samples become absorbing (Figs. 2 and 3 and Fig. S3). These phenomena can be collectively ascribed to an increase in sample emissivity at a critical power and a corresponding enhancement of heating laser and probe absorption in the sample (10). The correlation between optical changes in the visible (450–700 nm) and laser absorption changes in the infrared (1,075 nm), together with extrapolations of visible absorption spectra (e.g., Fig. 2*E*), indicate that absorptivity in the near IR is similar to that in the visible at the presently examined conditions. Thermal emission behavior differences are alone a robust criterion for determining sample optical character. The critical absorptivity of 0.1 μm^{-1} (optical depth of 10 μm) is roughly the

detection limit for absorbing conditions, above which sample transformation was clearly evident.

Character of Optical Transformations

The above phenomena require that an optically thick sample region forms between the incident laser and the foil (which initially acts as the laser heating coupler) when the sample transforms, such that bulk emissivity and absorptivity are substantially altered. Optical penetration depths ($1/\alpha$) as low as ~1 μm are measured in absorbing samples, consistent with this conclusion. Thus, for absorbing samples, emission can emerge dominantly from the hot sample, rather than the foil. Finite element models (Fig. 1 and Fig. S3) confirm that transference of laser heating from the foil to the sample and emission from the sample can describe features of the data that would otherwise be unexplained, such as long temperature plateaus despite decreasing laser heating power (Figs. 2 and 3). Transparent sample adjacent to absorbing sample (i.e., Fig. 1*C*) does not contribute to emission or absorption, so emission temperatures are those of the absorbing state.

For Ne, Ar, and Xe, an increase in temperature at the onset of absorbing states produced an observable gap in achieved temperatures (Figs. 4 and 5); absorbing conditions are interpreted to begin just above the highest-temperature transparent states, such that experiments achieving this critical temperature shift to higher temperatures while absorption increases (10). He, although showing most of the characteristic differences between transparent and absorbing conditions seen in Ne, Ar, and Xe, was particularly difficult to heat into an absorbing state, requiring the use of higher peak laser power (300 W for He compared with 200 W or less for other noble gases) as well as improved coupler thermal insulation. He also showed a continuous transition between transparent and absorbing conditions as well as a high-temperature experimental outlier showing no detectable absorption enhancement. These features can be explained by a difficulty in forming a sufficiently thick hot layer in the He sample, which may result from a low thermal conductivity in hot He compared with other noble gases or from use of a particularly short laser pulse in the He experiments (Fig. 3, compare with Fig. 2) to maximize protection of the anvils; the high-temperature outlier is thus interpreted as a case where the coupler was overheated due to insufficient growth of an absorbing He layer.

Although heating of the coupler surface (Fig. 3) produced absorbing states for all samples, heating of holes (Figs. 1 and 2) did not for He, Ne, and Ar at 22 GPa. We attribute this to the higher transformation temperatures for these samples, laser energy loss in holes, necessary use of broader laser focal spots for holes, and more regular damage to anvils for hole heating that limited the possible number of heat cycles. This limited transmission probing measurements to a maximum temperature of ~8,000 K.

For transmission probing (Fig. 1), temperatures were typically detectable only when samples became absorbing because the directly heated surface of the foil was not observed in the spectrogram and because sample inside the hole, while hot, did not emit if transparent. For transparent samples in transmission probing, temperature could be measured in a subsequent experiment that observed the directly heated surface around the hole from the opposite side of the cell but without TAS, requiring data from two heat cycles (or more) to establish temperature and optical character at given heating conditions. Reflection probing (Fig. 3) was superior for determining the character of transparent

states as it needed observations during only a single heat cycle. However, reflection probing was frequently complicated by probe beam interference between the foil and anvil. For example, interference fringes with a period of ~13 nm appear in the TAS-bb probe in Fig. 3, corresponding to a foil-to-anvil distance of ~10 μm given the He index of refraction (11) and fringe position shifts during the heat cycles. TAS-bb probe intensity was integrated across fringes in the spectra to remove contributions of fringe shift to the signal. TAS-cw probing was not used when interference was observed, as interference changes often dominated the signal and could not be readily removed from the data.

Foil reflectivity (emissivity) changes with temperature could in principal produce spurious signal changes in reflection TAS (Fig. 3). However, over the wide range of temperatures measured in transparent samples in this study, no systematic effects attributable to temperature-dependent emissivity were observed, indicating that any transient emissivity changes were small and within measurement noise. This is consistent with the known insensitivity of Ir emissivity to temperature (12). It is also not physically plausible that a metal's emissivity could increase enough to produce the observed transient extinctions: for extinctions of 90%, Ir emissivity would have to increase from around 0.3 to more than 0.9.

Sample Stability During Heating

Pressure (13) was examined before and after experiments, and showed no significant changes due to heating. Samples were also monitored with visual observations and Raman scattering. The foil sometimes showed evidence of deforming upon heating, as the appearance of surfaces or holes changed. These changes were sometimes manifested in the in situ probe observations as a permanent, rather than transient, signal change, of a small magnitude (up to several tens of percent) and positive or negative, which could occur at all temperatures. Such changes, when observed, were discriminable from those due to high sample absorption which were consistently transient, negative, and large in magnitude (>90%) and occurred only in conjunction with distinct change in the thermal emission response. Anvil damage (localized fractures or spots) was observed at the heated area occasionally, and thereafter a different part of the sample was studied. Raman scattering showed no evidence for chemical reactions between materials in the cell or graphitization of anvils. Xe, the most reactive of the noble gases studied, was also examined with synchrotron X-ray diffraction following heating, again showing no evidence for reaction.

Band Gaps of Noble Gases

Band gaps for noble gases Xe, Ar, and He were estimated from surveys of experimental (3–6, 14–17) and theoretical (18–23) results (Figs. S4–S7). The initial pressure in the sample gave its volume (5, 11, 24, 25), and temperature effects (particularly important for He) were estimated at this volume. In Fig. 5, the band gap for each pressure was estimated at the temperature of optical transformation to accurately locate the position of the transformation line. Volume changes with temperature in the experiments are small and have a negligible effect on the band gaps. Little is known about the gap of Ne under pressure and temperature, but it is expected to remain roughly constant under compression (26), so the ambient band gap (21.5 eV) (26) was used as an upper bound. For a lower bound, we assume a thermal shift in the gap similar to He (up to −10 eV at $T \sim 17 \times 10^3$ K; Fig. S6).

Because the band gaps of He and Ne are insensitive to compression (21–23, 26–28), the observed temperatures of optical opacity onset at modest density will be close to those at nearby densities. This ensures robust conclusions regarding noble gases for planetary and white dwarf interiors, where pure He and Ne would have densities close to those examined here (Figs. 4 and 5). Astrophysical models for He as a function of band gap

(Fig. 5) are based on planet models (29, 30) (Fig. 4) combined with the He equation-of-state (27) or on stellar models (31), with the gap calculated after ref. 21.

Optical Properties Analysis

In Figs. 2 E and F and 3 E and F, only random error in α is shown; systematic error due to thickness uncertainty (~50%) does not affect our conclusions.

For Ar (Fig. 2F), n was estimated from a fit to high-density index data (25, 32) ($n = 1.04 + 5.8/V$, where V is the volume in cm^3/mol) and included dispersion (32). Fitting Ar data (Fig. 2E) to the Urbach model, which can be written as

$$\alpha(\omega) = \alpha_0 \exp\left[-\frac{\gamma(E_g - \hbar\omega)}{kT}\right],$$ **[S1]**

where α_0 and γ are constants and kT/γ is the Urbach energy, yielded values of γ consistent with typical amorphous semiconductors (33). Tauc and indirect-gap semiconductor interband absorption models (15, 33), when fit to the Ar data (Fig. 2E), required negative values of the band gap, so these fits are not self-consistent or consistent with the known finite band gap at these conditions (Fig. S6) and nonmetallic conductivity (Fig. 2F).

The semiconductor free electron (Drude) model used in this study—see refs. 3, 21 and references therein—requires several choices in its parameterization. The effective carrier mass (m_{eff}) is taken as 2/3 the electron mass (m_e), consistent with prior fits of this model to measurements ($m_{eff} = 0.62 m_e$) (3) and theory ($m_{eff} = 0.61 m_e$) (21) on He and our fit of this model to optical data on Xe (15) ($m_{eff} = 0.71 m_e$). The bound electron contribution to the dielectric constant (ε_b) is taken as $\varepsilon_b = n^2$, where n is the value under pressure measured in He (11), Ne (11), Xe (24), and Ar as discussed above. Interatomic distance is taken from the equations of state (5, 11, 24, 25).

Correlation Between Electronic and Miscibility Changes in the H–He System

The H–He system can be divided into two regimes relevant to the present study. Above ~100 GPa, hydrogen undergoes a sharp transition to a metallic state at low temperature (34, 35) whereas He undergoes insulator–conductor transformation at higher temperatures (Fig. 4), with immiscibility predicted at least between these limits (34–36). Below ~100 GPa, hydrogen (37) and helium undergo electronic change over a broad and overlapping temperature range, and no high-temperature immiscibility is indicated (34–36). The boundary between these regimes occurs where the metallization transition of hydrogen sharpens and lowers in temperature (34, 35). Thus, at low pressures, there are no distinct conditions where hydrogen is metallic and helium is insulating, as is the case in the high-pressure immiscibility zone. Thus, high-temperature immiscibility is well correlated with the occurrence of contrasting electronic properties of constituents. Saturn's interior passes through the immiscibility zone and helium insulator–conductor transformation in the high-pressure region, where the relative electronic properties of constituents have a simple description, whereas Jupiter's interior remains close to the boundary between these regimes.

Thickness of Noble Gas Layer Above Saturn's Core

A noble gas layer above Saturn's core could represent a large structural feature of the planet's interior if composed of He (29, 38). A He-deficient, Ne-rich layer would be thinner but could still play a role in controlling chemical interactions at the core–envelope boundary. An upper bound on Ne layer thickness can be estimated assuming complete sedimentation of Ne from a primordial solar atmospheric concentration. Layer volume is

$$V_{\text{layer}} \approx 4\pi r^2 dr, \qquad \text{[S2]}$$

where r is the radius of the core–envelope boundary and dr is the layer thickness, assumed small. Layer volume may also be written as the volume fraction of Ne in the primordial envelope

$$V_{\text{layer}} \approx \frac{4}{3}\pi\left(R^3 - r^3\right)C, \qquad \text{[S3]}$$

where R is the planetary radius and C is the concentration by volume. Taking $r \equiv fR$,

$$dr \approx \frac{1}{3}CR\left(\frac{1-f^3}{f^2}\right). \qquad \text{[S4]}$$

For Saturn, $R = 6 \times 10^4$ km and $f = 0.15$. Then for an initial solar composition of $C = 0.0001$, $dr \approx 90$ km, or 0.15% of Saturn's radius.

1. Goncharov AF, et al. (2009) Laser heating in diamond anvil cells: Developments in pulsed and continuous techniques. *J Synchrotron Radiat* 16(6):769–772.
2. Dudley JM, Genty G, Coen S (2006) Supercontinuum generation in photonic crystal fiber. *Rev Mod Phys* 78(4):1135–1184.
3. Celliers PM, et al. (2010) Insulator-to-conducting transition in dense fluid helium. *Phys Rev Lett* 104(18):184503.
4. Kuhlbrodt S, et al. (2005) Electrical conductivity of noble gases at high pressures. *Contrib Plasma Phys* 45(1):61–69.
5. Ross M, Mao HK, Bell PM, Xu JA (1986) The equation of state of dense argon: A comparison of shock and static studies. *J Chem Phys* 85(2):1028–1033.
6. Fortov VE, et al. (2003) Pressure-produced ionization of nonideal plasma in a megabar range of dynamic pressures. *J Exp Theor Phys* 97(2):259–278.
7. Urlin VD, Mochalov MA, Mikhailova OL (1992) Liquid xenon study under shock and quasi-isentropic compression. *High Pressure Res* 8(4):595–605.
8. Reinholz H, et al. (2003) Frequency-dependent reflectivity of shock-compressed xenon plasmas. *Phys Rev E* 68(3 Pt 2):036403.
9. Goncharov AF, et al. (2012) Thermal conductivity of argon at high pressures and high temperatures. *J Appl Phys* 111(11):112609.
10. Boehler R, Ross M, Boercker DB (1997) Melting of LiF and NaCl to 1 Mbar: Systematics of ionic solids at extreme conditions. *Phys Rev Lett* 78(24):4589–4592.
11. Dewaele A, Eggert JH, Loubeyre P, Le Toullec R (2003) Measurement of refractive index and equation of state in dense He, H2, H2O, and Ne under high pressure in a diamond anvil cell. *Phys Rev B* 67(9):094112.
12. Hansen GP, Krishnan S, Hauge RH, Margrave JL (1989) Ellipsometric method for the measurement of temperature and optical constants of incandescent transition metals. *Appl Opt* 28(10):1885–1896.
13. Mao HK, Xu J, Bell PM (1986) Calibration of the ruby pressure gauge to 800 kbar under quasi-hydrostatic conditions. *J Geophys Res* 91(B5):4673–4676.
14. Asaumi K, Mori T, Kondo Y (1982) Effect of very high-pressure on the optical-absorption edge in solid Xe and its implication for metallization. *Phys Rev Lett* 49(11):837–840.
15. Goettel KA, Eggert JH, Silvera IF, Moss WC (1989) Optical evidence for the metallization of xenon at 132(5) GPa. *Phys Rev Lett* 62(6):665–668.
16. Steinberger IT, Asaf U (1973) Band-structure parameters of solid and liquid xenon. *Phys Rev B* 8(2):914–918.
17. Baldini G (1962) Ultraviolet absorption of solid argon, krypton, and xenon. *Phys Rev* 128(4):1562–1567.
18. Ross M, McMahan AK (1980) Condensed xenon at high-pressure. *Phys Rev B* 21(4):1658–1664.
19. Kwon I, Collins LA, Kress JD, Troullier N (1995) First-principles study of solid Ar and Kr under high compression. *Phys Rev B* 52(21):15165–15169.
20. Ross M (1968) Shock compression of argon and xenon. IV. Conversion of xenon to a metal-like state. *Phys Rev* 171(3):777–784.

21. Soubiran F, Mazevet S, Winisdoerffer C, Chabrier G (2012) Helium gap in the warm dense matter regime and experimental reflectivity measurements. *Phys Rev B* 86(11):115102.
22. Kowalski PM, Mazevet S, Saumon D, Challacombe M (2007) Equation of state and optical properties of warm dense helium. *Phys Rev B* 76(7):075112.
23. Stixrude L, Jeanloz R (2008) Fluid helium at conditions of giant planetary interiors. *Proc Natl Acad Sci USA* 105(32):11071–11075.
24. Makarenko I, Weill G, Itie JP, Besson JM (1982) Optical observations on xenon up to 63 GPa. *Phys Rev B* 26(12):7113–7115.
25. Hanna GJ, McCluskey MD (2010) Equation of state and refractive index of argon at high pressure by confocal microscopy. *Phys Rev B* 81(13):132104.
26. He YG, Tang XZ, Pu YK (2010) First-principle study of solid neon under high compression. *Physica B* 405(20):4335–4338.
27. Militzer B (2009) Path integral Monte Carlo and density functional molecular dynamics simulations of hot, dense helium. *Phys Rev B* 79(15):155105.
28. Boettger JC (1986) Equation of state and metallization of neon. *Phys Rev B* 33(10):6788–6791.
29. Nettelmann N, Pustow R, Redmer R (2013) Saturn layered structure and homogeneous evolution models with different EOSs. *Icarus* 225(1):548–557.
30. Nettelmann N, Becker A, Holst B, Redmer R (2012) Jupiter models with improved ab-initio hydrogen equation of state. *Astrophys J* 750(1):52.
31. Bergeron P, Saumon D, Wesemael F (1995) New model atmospheres for very cool white-dwarfs with mixed H/He and pure He compositions. *Astrophys J* 443(2):764–779.
32. Sinnock AC, Smith BL (1969) Refractive indices of condensed inert gases. *Phys Rev* 181(3):1297–1307.
33. Mott NF, Davis EA (1979) *Electronic Processes in Non-Crystalline Materials* (Clarendon Press, Oxford), 2nd Ed.
34. Lorenzen W, Holst B, Redmer R (2009) Demixing of hydrogen and helium at megabar pressures. *Phys Rev Lett* 102(11):115701.
35. Morales MA, Hamel S, Caspersen K, Schwegler E (2013) Hydrogen-helium demixing from first principles: From diamond anvil cells to planetary interiors. *Phys Rev B* 87(17):174105.
36. Morales MA, et al. (2009) Phase separation in hydrogen-helium mixtures at Mbar pressures. *Proc Natl Acad Sci USA* 106(5):1324–1329.
37. Collins LA, et al. (2001) Dynamical and optical properties of warm dense hydrogen. *Phys Rev B* 63(18):184110.
38. Guillot T (2005) The interiors of giant planets: Models and outstanding questions. *Annu Rev Earth Planet Sci* 33:493–530.
39. Kietzmann A, Holst B, Redmer R, Desjarlais MP, Mattsson TR (2007) Quantum molecular dynamics simulations for the nonmetal-to-metal transition in fluid helium. *Phys Rev Lett* 98(19):190602.
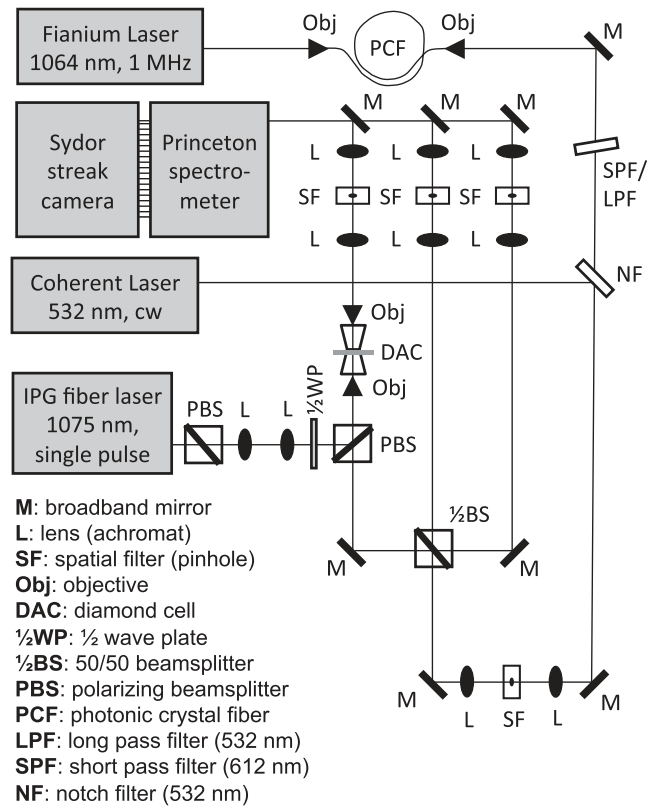
Fig. S1. Principal elements of experimental apparatus. Broadband supercontinuum (1 MHz, 150-ps pulse duration) was created by pumping a photonic crystal fiber (PCF) with a 1,064-nm fiber laser (1 MHz, 10-ps pulse duration; Fianium Ltd.). This was filtered spectrally to create a sharp edge to the spectrum (at 532 or 612 nm) and combined with a 532-nm cw laser beam (Coherent Verdi) using a notch filter in reflection mode, creating a combined beam for transient absorption spectroscopy (TAS). These sources were precisely overlapped at a spatial filter (Lens + Pinhole + Lens) and in the diamond cell, where they were further overlapped with the heating laser (1,075 nm, electrically modulated to several μs duration; IPG Photonics), which was focused to a spot of desired size using a telescope (pi-Shaper; AdlOptica GmbH) and power-modulated using polarization techniques. Imaging at the diamond anvil cell (DAC) was achieved with fast objectives (Mitutoyo NIR 20× NA 0.4). The output of the TAS signal in transmission or reflection, together with emission background, passes through a spatial filter system before entering the spectrometer. Also, a reference beam for TAS measurements could be delivered to the spectrometer. The beams entering the detector were selected using a system of switching mirrors, and two beams could enter at a given time.
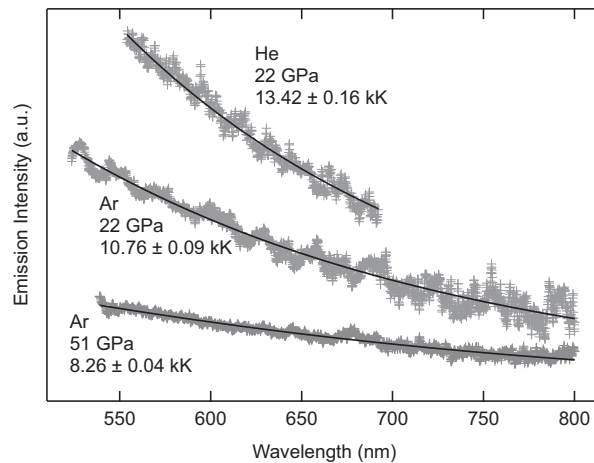

Fig. S2. Snapshots of emission spectra with grey body Planck fits. Emission was taken from 0.5- to 1-μs time windows on the spectrogram; this defined the time resolution of the data. For Ar (lower curves), data from 2 to 10 identical heat cycles using two to three spectral bands were integrated together, with a time resolution of 0.5 μs. Such integrated cycles were first determined to have highly similar character, so that they could be combined and averaged. For He (upper curve), data were taken from one shot and a time resolution of 1 μs. Effective total integration times for emission in these examples thus range from 0.5 to 4 μs. Relative curve intensities are arbitrary. Emission was referenced to a NIST-traceable tungsten filament standard lamp. Uncertainties are least-squares fitting error.
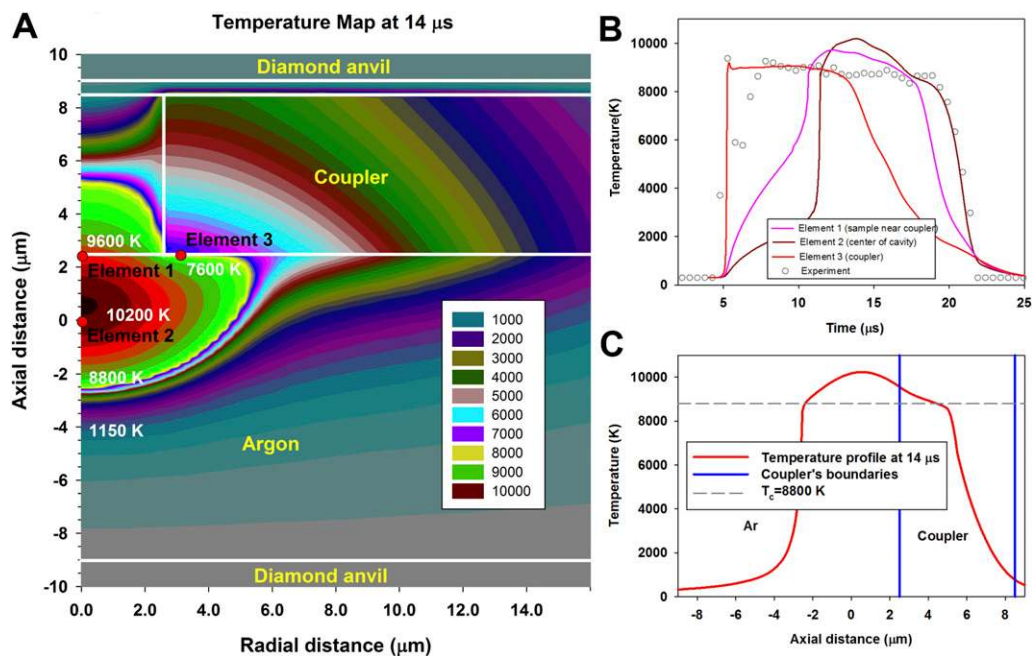
Fig. S3. Finite element simulation of experiment in Ar at 51 GPa. (*A*) Temperature map of sample cavity ~9 μs after heating begins, showing the transference of laser heating from the foil (coupler) to the sample and cooling of the foil due to screening by absorptive sample near the foil hole. (*B*) Temperature evolution at selected points in *A* compared with observed temperatures. The model reproduces the long temperature plateau, steep drop in temperature late in the heat cycle, and decoupling from laser power (Fig. 2*B*); these features could only be reproduced assuming the sample became absorbing at high temperature and not if a transparent sample was assumed. (*C*) Axial temperature profile for *A* showing temperature changing sharply across transparent regions, accommodating a large temperature drop between heated sample and diamond anvils, whereas temperature is relatively uniform in the absorbing sample region due to distributed laser heating. Simulation parameters appropriate for Ar, diamond, and the metal foil were used (9), with the Ar thermal conductivity K modified at high temperatures as $K/K_r = (300/T)^{1.5} + f_1\{erf[(T - T_c)/T_w] + 1\}$ and Ar absorption introduced as $\alpha/\alpha_r = \{erf[(T - T_c)/T_w] + 1\}[f_2(T/T_c) - 1]$, where T is in K. Direct laser heating of each Ar cell accounted for local absorption and the screening of the laser in adjacent cells, as well as beam reflections from the coupler. The parameters $K_r = 100$ W/mK, $\alpha_r = 2 \times 10^5$ m^{-1}, $T_w = 300$ K, $T_c = 8800$ K, $f_1 = 0.175$, and $f_2 = 1.25$ were adjusted to reproduce observed time histories of temperature (*B*) and probe absorption (Fig. 2).
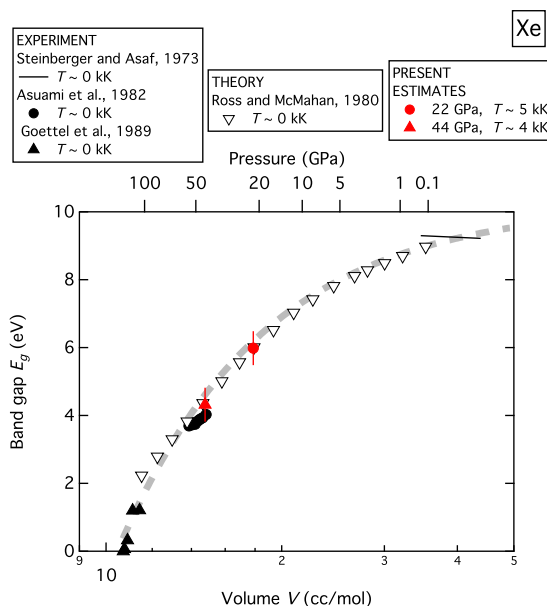

Fig. S4. Band gap of xenon. Experimental data (14–17) and a theoretical prediction (18) show the well-known closure of the gap at ~132 GPa. Shock wave data at high temperature are well described by band gaps consistent with these estimates (18). Present estimates for the gap at transformation are filled red points. The band gap is modeled as $E_g(V) = 10.2 - 601\ V^{-1.74}$ (gray dashed curve, E_g in eV, V in cm^3/mol). Pressure is given by the static isotherm (24).
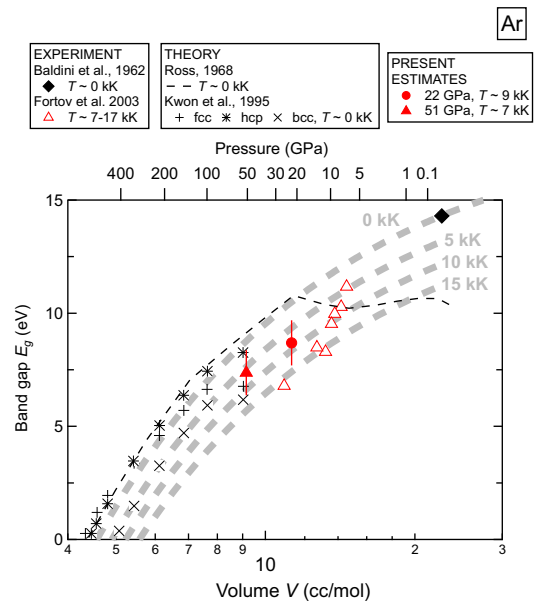
Fig. S5. Band gap of argon. The gap has been measured near ambient conditions (17). The gap at extreme conditions (open triangles) was modeled after measurements of conductivity, temperature, and density under shock compression (4–6) assuming semiconductor excitation behavior (3, 21); this model was in turn used to determine the DC conductivity for Ar in Fig. 2F. Theoretical predictions at low temperature (19, 20) are consistent with experimentally determined values but fall to somewhat higher E_g, consistent with a modest temperature effect on the gap; this is accounted for in our estimates for E_g at transformation conditions (filled red points). The band gap is modeled as $E_g(V, T) = 18.5 - 75.6\ V^{-0.926} - 0.000527\ T^{0.902}$ (gray dashed curves, E_g in eV, V in cm^3/mol, T in K). Pressure is given by the static isotherm (5, 25).
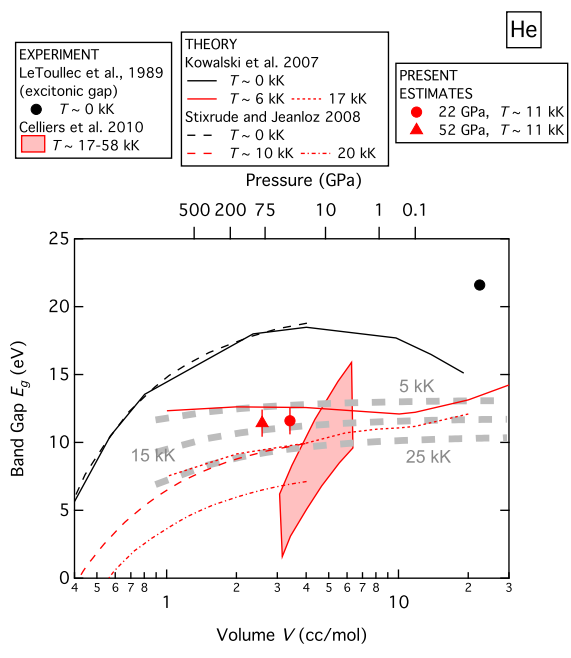

Fig. S6. Band gap of helium. Experimental data on the gap (3) include the range due to uncertainty (red outlined region) and fall to higher temperatures than examined here but at similar volume. The excitonic gap near ambient conditions (3), which represents a close approximation (lower bound) to the band gap (17), is also shown. Theoretical results for the gap (21–23, 27, 39) show strong temperature sensitivity at constant volume. Estimates for our experiments near $T \sim 11 \times 10^3$ K (filled red points) are selected consistent with the model of ref. 21. This model has been shown to be consistent with experiments (3) and first-principles theory (22) and is given by $E_g(V,T) = 13.8 - 32.5/V\ (1/38.5 + T/348,000) - T/7470$ (gray dashed curves, E_g in eV, V in cm^3/mol, T in K). This model is also used to describe He in planetary and stellar interiors (Fig. 5). Estimates from this model fall somewhat above the theoretical results of ref. 23, where calculations are systematically low possibly due to neglecting localization in the fluid density of states (23), as discussed in the main text. Pressure is given by the static isotherm (11).
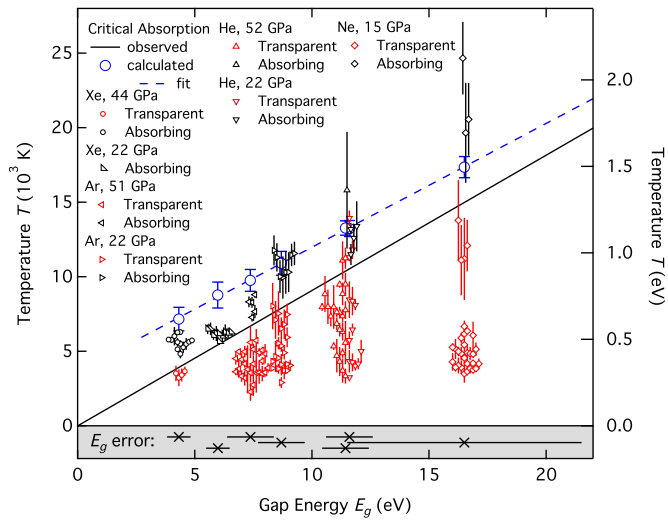
Fig. S7. Detail of Fig. 5. Optical properties of noble gases at 450–1,075 nm. Present data from Fig. 5 are shown with results at a given band gap distributed artificially in the horizontal direction to reveal the character of individual experiments. Temperature uncertainties for a given shot include uncertainty in instantaneous temperature and temporal variations in temperature (Figs. 2 and 3). At the bottom of the plot, band gap values for each sample are shown together with uncertainty. Dashed blue line is the onset of critical absorption for free electron behavior (3, 21) and is a linear fit to specific predictions made for each sample (blue circles, with bars covering range of predictions in this spectral range; *SI Text*); the fitted line is terminated at the band gap where interband absorption effects should appear in this spectral range.